ORIGINAL ARTICLE

Graphitic carbon nitride loaded with bismuth nanoparticles displays antibacterial photocatalytic activity

Hui Zhang* , Ling Li, Qian-Qian Li, Tao Ma, Jia-Qi Gao, Jin-Bo Xue, Shuang Gao

Abstract Metal-free graphitic carbon nitride nanomaterials have been widely applied in the medical antibacterial field owing to their high anisotropy, excellent stability, satisfactory biocompatibility, and non-toxicity. Herein, Bi/C_3N_4 nanocomposites were successfully constructed by hydrothermal method followed by loading bismuth on the surface of graphite carbon nitride. Bi nanospheres were tightly combined with the layered g-C_3N_4 surface to promote effective separation of photo-induced charges, which results in the Bi/C_3N_4 composite material that exhibited excellent photocatalytic activity under visible light. In addition, the surface plasmon resonance characteristics of semi-metal Bi further enhanced the visible-light absorption of the Bi/C_3N_4. However, excessive Bi may inhibit the light-trapping ability of Bi/C_3N_4. 1.0% Bi/C_3N_4 demonstrates excellent bactericidal efficiency as high as 96.4% against *Escherichia coli* (*E. coli*), which is attributed to the promotion of the production of reactive oxidative species. The enhanced mechanism of Bi/C_3N_4 synergistically achieving enhanced photocatalytic antibacterial activity under the coupling of multiple advantages was clarified, providing theoretical guidance for its application in the field of water disinfection and antibacterial treatment.

H. Zhang*, L. Li, Q.-Q. Li
Department of Plastic Surgery, Second Hospital of Shanxi Medical University, Taiyuan 030001, China
e-mail: zhengxingzh1@126.com

T. Ma, J.-Q. Gao, J.-B. Xue
Key Laboratory of Interface Science and Engineering in Advanced Materials, Taiyuan University of Technology, Ministry of Education, Taiyuan 030024, China

S. Gao
Department of Materials and Earth Sciences, Technical University of Darmstadt, Darmstadt 64287, Germany

1 Introduction

Diseases caused by bacterial infections pose a serious threat to human health. Generally, antibiotics are widely used to treat infections, but their abuse has resulted in drug resistance and the occurrence of super bacteria [1, 2]. Therefore, it is imperative to develop more effective sterilization techniques that do not involve antibiotics [3]. Compared with traditional sterilization methods, such as chemical drug delivery and ultraviolet inactivation, photocatalytic technology based on semiconductor materials has been identified as an innovative sterilization method [4, 5]. Photocatalytic sterilization is an efficient, safe, and environmentally friendly technology. The strong oxidizing ability of active oxygen groups generated by semiconductors under light can cause oxidation of phospholipids and proteins and destroy bacterial cell membranes, thereby inactivating bacteria effectively [6].

For constructing photocatalysts, two-dimensional (2D) materials have been widely used in the field of nanomedicine, due to their high anisotropy and chemical functions. Among them, the 2D nanomaterial g-C_3N_4 exhibits both green and non-toxic superiorities. All these characteristics make it a biomedical material with unique advantages [7, 8]. Under light, the photogenerated electrons in the conduction band of g-C_3N_4 react with O_2 molecules to form superoxide radicals ($\cdot O_2^-$). The photogenerated holes in the valence band can oxidize water or hydroxides to form hydroxyl radicals ($\cdot OH$). $\cdot O_2^-$, $\cdot OH$, and h^+ can all be used as oxidative active species, which can interact with

bacteria in the environment and inactivate them by oxidation [9]. By modulating the band gap, electronic structure, and carrier separation efficiency of g-C$_3$N$_4$, the photocatalytic antibacterial efficiency can be optimized. To date, many studies have confirmed the excellent properties of g-C$_3$N$_4$ and its potential applications [10–13].

It is widely known that one of the keys to achieving high-efficiency photocatalysis is to inhibit the recombination of light-excited carriers [14–20]. Currently, noble metals are loaded onto the surface of g-C$_3$N$_4$ to promote the separation of photogenerated charges [21, 22]. The coupling of the semiconductor with the metal nanoparticle can construct a Schottky barrier at the interface to further accelerate the separation and transfer of photogenerated charges in the composite. The generated photoelectrons can be quickly transferred to the metal nanoparticle for accumulation, while leaving holes on the semiconductor surface [23]. It has been reported that g-C$_3$N$_4$ modified with silver nanoparticles shows excellent antibacterial activity [24]. Although silver nanoparticles show favorable bactericidal properties, the released silver ions are toxic and pollute the environment [25]. Therefore, it is necessary to develop alternative metal antibacterial additives.

Low-cost and easy-to-obtain semi-metal bismuth has been recognized as an ideal substitute for precious metals due to its good photocatalytic activity [26]. The role of bismuth as an antibacterial agent has been confirmed. Bismuth is generally believed to be a metal with relatively low toxicity in humans. Several bismuth compounds have been reported to remove Helicobacter pylori [27]. Bismuth can act as an electron trap, accelerating the separation of charges at the interface by forming a Schottky barrier. Simultaneously, the semi-metal Bi also exhibits surface plasmon resonance (SPR) characteristics, which can enhance the absorption of visible light and the local electric field to activate more carriers. Therefore, in this work, biloading of graphitic carbon nitride was designed to obtain a photocatalyst with high carrier separation efficiency, wide visible-light response range, and consequently excellent antibacterial performance. The antibacterial performance toward *Escherichia coli* was tested by inactivation measurements.

2 Experimental

2.1 Materials

Melamine (C$_3$H$_6$N$_6$, 99.5%) was purchased from Tianjin Guangfu Chemical Reagent Co., Ltd. Bismuth nitrate (Bi(NO$_3$)$_3$·5H$_2$O, 99.0%) was purchased from Sinopharm Chemical Reagent Co., Ltd. Polyvinylpyrrolidone ((C$_6$H$_9$NO)$_n$, 95.0%) was purchased from Tianjin Guangfu

Fine Chemical Research Institute. Deionized water was prepared and used in all experiments.

2.2 Photocatalyst preparation

Pristine g-C$_3$N$_4$ was prepared using the traditional thermal polycondensation method. Typically, 3 g melamine was annealed in a tube furnace at 550 °C in air for 2 h (at a heating rate of 4 °C·min^{-1}), ground, and sifted with 300 mesh sieves to obtain granular g-C$_3$N$_4$ powder.

According to a previous study [28], with a slight change in procedure, Bi was loaded onto g-C$_3$N$_4$ by a hydrothermal method (Scheme 1). First, 10 ml 1mol·L^{-1} HNO$_3$ was added to 50 ml ethylene glycol under stirring, and then a certain amount of Bi(NO$_3$)$_3$·5H$_2$O and 1 g polyvinylpyrrolidone (PVP, molecular weight approximately 58,000) was added to the solution and stirred until complete dissolution. Then, 0.1 g g-C$_3$N$_4$ powder was dispersed in the solution, stirred for 30 min, and then sonicated for 3 min to ensure that the powder and solution were evenly mixed. The suspension was poured into a reactor and kept at 160 °C for 24 h. After cooling to room temperature, the product was removed for centrifugal separation, washed several times, and finally dried at 50 °C for 24 h to obtain Bi-loaded g-C$_3$N$_4$. Four dosages (0.0027, 0.0053, 0.0106 and 0.0265 g) of Bi(NO$_3$)$_3$·5H$_2$O were used to obtain Bi-loaded g-C$_3$N$_4$ samples with molar ratios of Bi to g-C$_3$N$_4$ of 0.5%, 1.0%, 2.0% and 5.0%. The samples were labeled as 0.5% Bi/C$_3$N$_4$, 1.0% Bi/C$_3$N$_4$, 2.0% Bi/C$_3$N$_4$ and 5.0% Bi/C$_3$N$_4$.

2.3 Characterization

Field emission scanning electron microscopy (FESEM, JEOL JSM-6700F) and high-resolution transmission electron microscopy (HRTEM, JEOL JEM-2100F) were used to observe the morphology and microstructure of Bi/C$_3$N$_4$ samples; meanwhile, energy-dispersive spectroscopy (EDS) measurements were taken. The crystalline structure of the catalysts was examined by X-ray diffraction (XRD, DX-2700X) with Cu Kα irradiation ($\lambda = 0.15406$ nm) operating at 40 kV and 30 mA in the 2θ range from 10° to 80° with a 0.02° scan step size. The functional groups were analyzed by Fourier transform infrared spectrometry (FTIR, NICOLET AVATAR 330) using KBr pellets in the wave number range between 4000 and 500 cm^{-1}. Ultraviolet–visible (UV–Vis) diffused reflectance spectra of the powder samples coated on FTO were recorded by UV–Vis spectrophotometry (UV–Vis, PerkinElmer Lambda950) using BaSO$_4$ sample disk to remove the substrate. Steady-state fluorescence spectra were measured with a photoluminescence spectrometer (PL, F900) under an excitation wavelength of 350 nm. A self-assembled surface
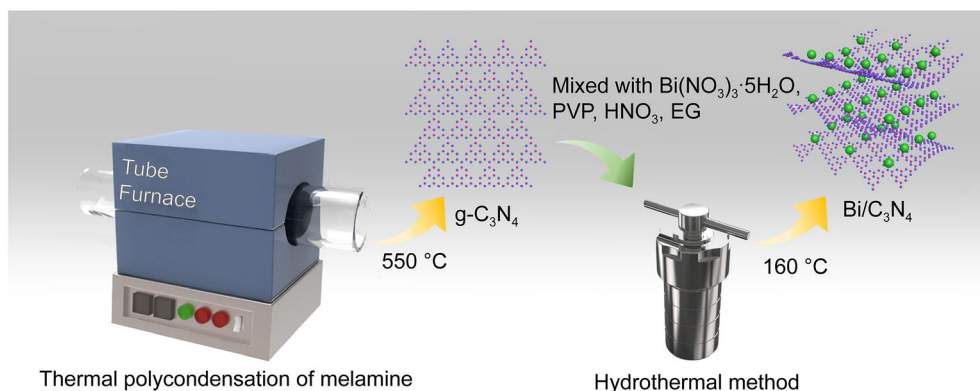
Scheme 1 Schematic diagram of synthesis process and preparation flow of Bi-loaded g-C$_3$N$_4$ (Bi/C$_3$N$_4$)

photovoltaic (SPV) system based on a lock-in amplifier (Model SR830-DSP) synchronized with a light chopper was applied to detect the photovoltaic signal.

2.4 Photoelectrochemical property test

The electrochemical tests were carried out on an AutoLab electrochemical workstation incorporating a 300-W xenon lamp source. A three-electrode system was employed in all tests. The catalyst powder (0.01 g) was ground together with Nafion (10 μl) and deionized water (100 μl) and then coated on a glassy carbon electrode and treated at 50 °C for 3 h to obtain the working electrode. Pt plate and saturated calomel electrode (SCE) were used as the counter electrode and reference electrode, respectively, and a 0.5 mol·L^{-1} NaSO$_4$ solution was used as the electrolyte. Transient photocurrent measurements were taken in the dark environment with 100 mW·cm^{-2} illumination at 0 V (vs. SCE) bias voltage. Electrochemical impedance spectroscopy (EIS) measurement frequency range is from 0.01 to 100,000 Hz, and for Mott–Schottky measurement, it is stable at 1000 Hz.

2.5 Antibacterial photocatalytic performance

The photocatalytic disinfection activity of each sample was evaluated using an inactivation test of *Escherichia coli* (*E. coli*). To obtain the inoculum, a single colony was placed in 10 ml Luria Bertani (LB) medium at 37 °C in a shaker overnight. Bacterial cells in the media were harvested by centrifugation, washed twice, and then diluted with sterile phosphate buffer (PB, 0.1 mol·L^{-1}, pH 7.0) to 1×10^3 colony-forming units·ml^{-1} (CFU·ml^{-1}). In the photocatalytic disinfection test, 10 mg photocatalyst was added to 3 ml *E. coli* suspension buffer and stirred for 10 min at 300×10^{-6} before light irradiation (the non-irradiated reference remained in the dark). A 300-W xenon lamp (CHF-XM300W, Perfect Light, China) with a UV-

CUT filter ($\lambda \geq 420$ nm) was used as a visible-light source, and the samples were illuminated for 1 h. Thereafter, aliquots of the samples (80 μl each) were spread onto LB plates and cultured at 37 °C for 18 h to form viable colony units. The inactivation rate of bacteria was calculated as C/C_0, where C_t and C_0 are the bacterial concentrations sampled at a certain time and before illumination, respectively.

2.6 In vitro cytocompatibility

2.6.1 Cell culture

Fibroblast was cultured in D-MEM supplemented with 10% FBS, 1% penicillin, and streptomycin at 37 °C under an atmosphere of 5% CO$_2$ and 95% air.

To assess the cell cytotoxicity, 1 μl of the cell suspension (2×10^4 cells·cm^{-2}) was inoculated in 24-well plates and cocultured with the extract of each sample and cell culture medium, and the cell culture medium was changed once a day.

2.6.2 Cell viability assay

In order to visually observe the viability of adherent cells on samples, a live–dead stain (calcein AM and EthD-1) was used. The cells on the samples were washed three times with PBS after 1 and 3 days. Then, 50 μl of the staining solution was dropped onto the samples and incubated for 1 h at 37 °C in the dark. Afterward, the green living cells and red dead cells were investigated by CLSM.

Cell proliferation was evaluated quantitatively by MTT (Sigma, the USA) assay. The osteoblasts were cultured for 1 and 3 days on 24-well plates, respectively. 900 μl D-MEM culture medium and 100 μl 5 mg·ml^{-1} MTT solution were added to samples and after 4 h, and the liquid on the 24-well plate was removed. Then, the samples were washed with 1 ml dimethyl sulfoxide (DMSO, Sigma, the USA) to dissolve the crystals. Finally, the optical density

(OD) of the solution was measured at 492 nm on a microplate reader (Infinite F50, TECAN).

3 Results and discussion

3.1 Morphology and structure

SEM and TEM images of g-C_3N_4 and $x\%$ Bi/C_3N_4 are shown in Fig. 1. The original g-C_3N_4 exhibits a layered structure, as shown in Fig. 1a. The morphology of $x\%$ Bi/C_3N_4 with different Bi loading levels was also observed. It can be clearly seen that g-C_3N_4 retained the original 2D structure when Bi nanospheres were loaded on it. As shown in Fig. 1b–e, the presence of Bi on the surface of the sample was also detected by EDS (Fig. 1f). The size of the Bi nanospheres ranged from tens to hundreds of nanometers. In addition, with the increase in the amount of Bi(NO_3)$_3 \cdot 5H_2O$ used in the preparation process, Bi loading showed a gradually increasing trend. With the highest loading of 5% Bi/C_3N_4, a large quantity of Bi nanospheres densely covered the surface of g-C_3N_4. TEM images of 1.0% Bi/C_3N_4 (Fig. 1g) also clearly show the presence of Bi nanospheres deposited on the surface of g-C_3N_4 that are tightly bonded to each other. A closer inspection shows that Bi nanospheres exhibit clear lattice stripes with a pitch of 2.17 nm, corresponding to the (110) crystal plane of Bi, as shown in HRTEM image (Fig. 1h).

XRD patterns of g-C_3N_4 and $x\%$ Bi/C_3N_4 are shown in Fig. 2a. g-C_3N_4 exhibited two typical diffraction peaks at
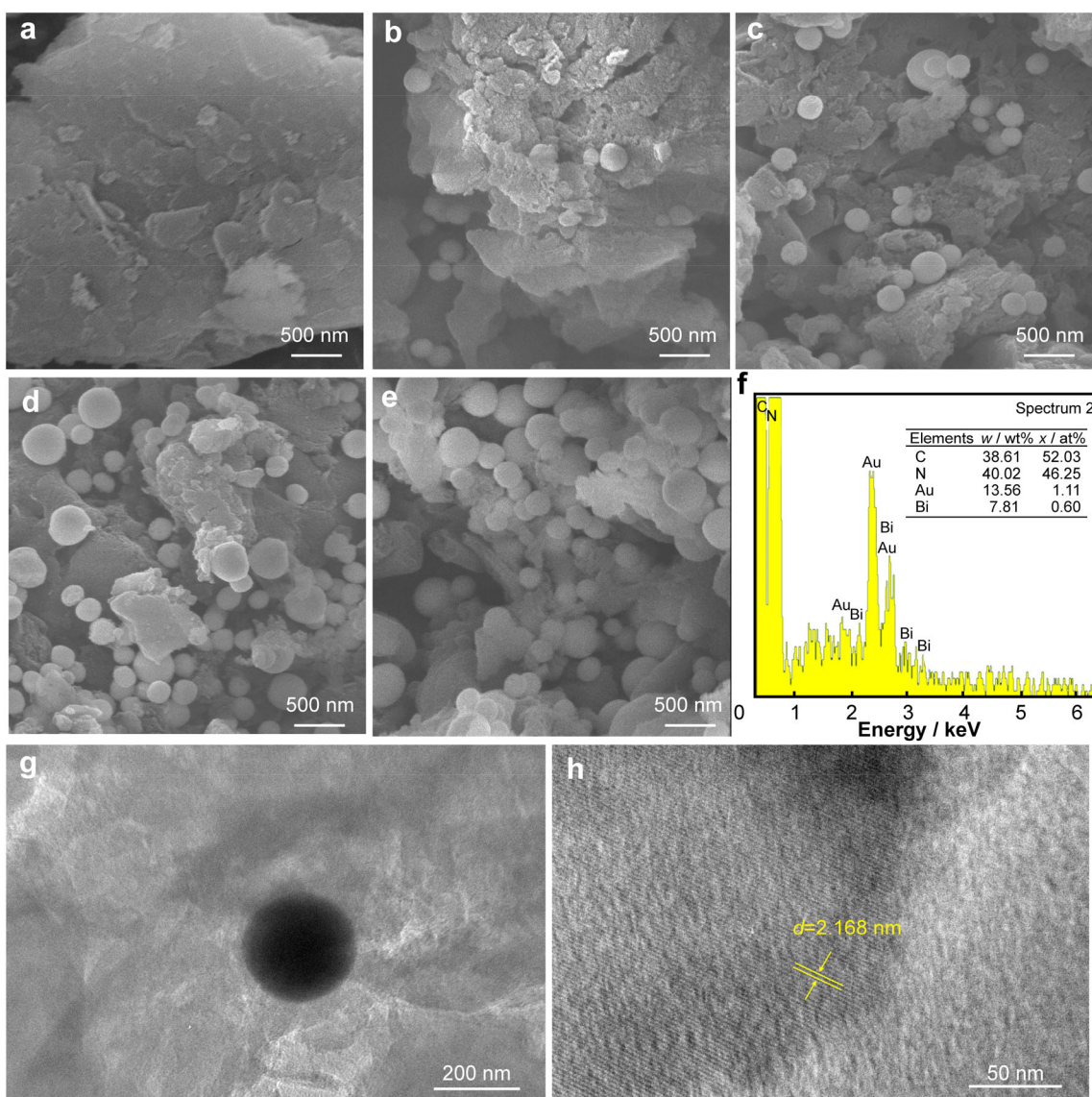
Fig. 1 SEM images of **a** g-C_3N_4, **b** 0.5% Bi/C_3N_4, **c** 1.0% Bi/C_3N_4, **d** 2.0% Bi/C_3N_4 and **e** 5.0% Bi/C_3N_4; **f** EDS results of 1.0% Bi/C_3N_4; **g** TEM and **h** HRTEM images of 1.0% Bi/C_3N_4
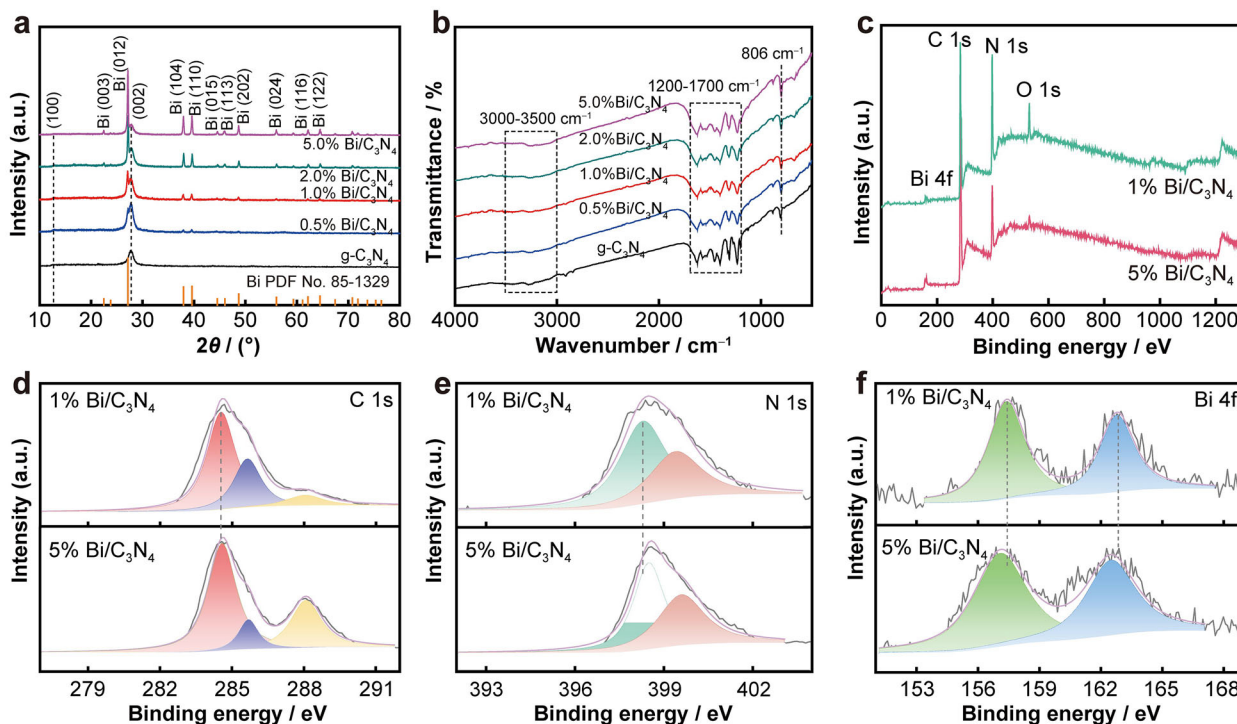
Fig. 2 **a** XRD patterns and **b** FTIR absorption spectra of g-C_3N_4 and x% Bi/C_3N_4; **c** full XPS survey spectra; **d** high-resolution XPS spectra of C 1s; **e** N 1s and **f** Bi 4f for 1.0% Bi/C_3N_4 and 5.0% Bi/C_3N_4

13.0° and 27.8°, corresponding to the (100) crystal plane caused by the in-plane repeating structural moieties and the (002) crystal plane caused by the π-conjugated planes in layered structures, respectively [29]. These two peaks were also observed for x% Bi/C_3N_4 samples, indicating that the hydrothermal treatment process did not affect the structure of g-C_3N_4. With the loading of Bi nanospheres, a series of new diffraction peaks appeared in x% Bi/C_3N_4, which corresponded perfectly to the characteristic peaks of elemental Bi (JCPDS No. 85–1329). In addition, no other impurity peaks were observed, revealing the formation of Bi nanospheres in the form of a simple substance. The peak intensity related to elemental Bi increased with an increase in the loading amount of Bi nanospheres. The diffraction peaks of Bi in the samples with a lower loading amount of Bi nanospheres were inconspicuous. This is because Bi nanospheres are present on g-C_3N_4 in very small numbers and in a highly dispersed state [30]. These results suggest that elemental Bi nanospheres were loaded on g-C_3N_4 with no BiO_x or other phases.

FTIR spectra of g-C_3N_4 and x% Bi/C_3N_4 are shown in Fig. 2b. All samples exhibited three strong absorption bands at 804, 1200–1700, and 3000–3700 cm^{-1} related to carbon nitride, which are attributed to the bending vibration of the heptazine ring, the stretching vibrations of C=N, C–N, and C–N outside the ring, and the stretching vibration of uncondensed amino groups –NH– and –NH_2 on the

edge of the aromatic ring and the water O–H adsorbed on the surface, respectively [31]. The characteristic bands of the x% Bi/C_3N_4 samples were almost unchanged after Bi loading, suggesting that the loading of Bi nanospheres on the surface of g-C_3N_4 did not change its characteristic structure.

The bonding states between the elements in the Bi-loaded samples were further analyzed by XPS. XPS full spectra of the high- and low-loading-capacity catalysts (1.0% Bi/C_3N_4 and 5.0% Bi/C_3N_4) (Fig. 2c) indicate the presence of C, N, O and Bi in the samples. The O species may be derived from O_2 or H_2O adsorbed on the surface of the material. Fig. 2d shows the C 1s energy level spectra, which can be deconvoluted into three peaks at 284.6, 285.6 and 288.1 eV. The peaks with a binding energy of 284.6 and 285.6 eV are attributed to the C–C bond of the sp^2 C atom bonded to the N atom and the sp^2 C atom attached to the –NH_2 group in the aromatic ring [32], respectively, while the peak at 288.1 eV is assigned to sp^2 hybridized carbon (N–C=N) [33]. The N 1s pattern in Fig. 2e can also be deconvoluted into two peaks at 398.4 and 399.5 eV. Of these, the peak at 398.4 eV is indexed to sp^2 hybrid nitrogen (C–N=C) and the peak at 399.5 eV is identified as the tertiary nitrogen group (N–$(C)_3$). The Bi 4f pattern (Fig. 2f) shows two peak positions with binding energy of 156.9 and 162.3 eV, both of which can be indexed as Bi simple substances [34]. As a whole, 5.0% Bi/

C_3N_4 exhibited a peak pattern similar to that of 1.0% Bi/C_3N_4, and XPS peak of Bi shifted to a low binding energy with the increase in loading concentration, which can be attributed to the transfer of electrons from the sp^2-hybridized p-conjugated g-C_3N_4 network to Bi. Bi accepts electrons, and this manifests an increase in electron cloud density. The above analysis proves that the Bi species mainly exist in the form of Bi simple substances, are loaded on the surface of g-C_3N_4 and interact with N atoms, and further promote charge transfer in the catalyst.

3.2 Optical properties

To characterize the light absorption performance of g-C_3N_4 and x% Bi/C_3N_4, UV–Vis absorption spectra were recorded, as shown in Fig. 3a. After the loading of Bi nanospheres, the light absorption capacity of the samples in the visible-light region was improved, and the light absorption band edge was significantly red-shifted and broadened, and the light absorption intensity gradually increased with Bi loading increasing, which explained the color of the samples gradually changing from light yellow to dark brown. This may be due to the charge transfer between the Bi nanospheres and g-C_3N_4 [35]. According to the Kubelka–Munk formula [36], the band gaps of the prepared materials were quantified, and the band gap values were estimated to be 2.79, 2.61, 2.59, 2.53 and 2.26 eV, corresponding to g-C_3N_4 and 0.5%–5.0% Bi/C_3N_4 samples, respectively, as shown in Fig. 3b. This significant change in the band gap reflects the change in the internal electronic structure of x% Bi/C_3N_4, which means that there was an electron exchange between g-C_3N_4 and supported Bi nanospheres [37] and also proves that the interaction between Bi and g-C_3N_4 results in the formation of a Schottky junction rather than a simple physical contact. It is widely known that semi-metallic Bi nanospheres with precious metal-like properties can exhibit SPR characteristics in the visible-light region,

which is also a critical reason for the increased absorbance of x% Bi/C_3N_4 in the visible-light region [29]. The improved light absorption capacity facilitated the photocatalytic antibacterial activity of Bi/C_3N_4 under visible light.

3.3 Carrier behavior evaluation

The separation efficiency of the photogenerated electron–hole pairs of g-C_3N_4 and x% Bi/C_3N_4 was analyzed by fluorescence spectroscopy, and the PL spectra with an excitation wavelength of 350 nm are shown in Fig. 4a. All samples exhibited two strong emission peaks centered at 438 and 465 nm, which are attributed to the quantum confinement effect and band gap transition of graphitic carbon nitride, respectively [38]. The intensity of the emission peak decreased significantly after Bi loading, indicating that the separation efficiency of the photogenerated carriers was improved. Loading increased levels of Bi nanospheres, which led to a higher separation efficiency. The main reason for this phenomenon is the formation of a Schottky junction at the interface of the Bi nanospheres and g-C_3N_4 [39]. According to reports [40], the Fermi level of semi-metal Bi is roughly at − 0.17 eV (vs. NHE), which is more positive than the bottom of the conduction band of g-C_3N_4. Therefore, the electrons generated under illumination on the conduction band of g-C_3N_4 can quickly migrate to the surface of the metal Bi, which can capture and transfer photogenerated electrons as an electron trap, thereby separating the photogenerated charges more effectively. Subsequently, the electrons accumulated on the surface of the Bi nanospheres are captured by the surrounding oxygen to form reactive oxidative species (ROS). Consequently, the photogenerated carrier separation efficiency of g-C_3N_4 can be further improved by loading Bi nanospheres to capture and consume the photogenerated electrons.
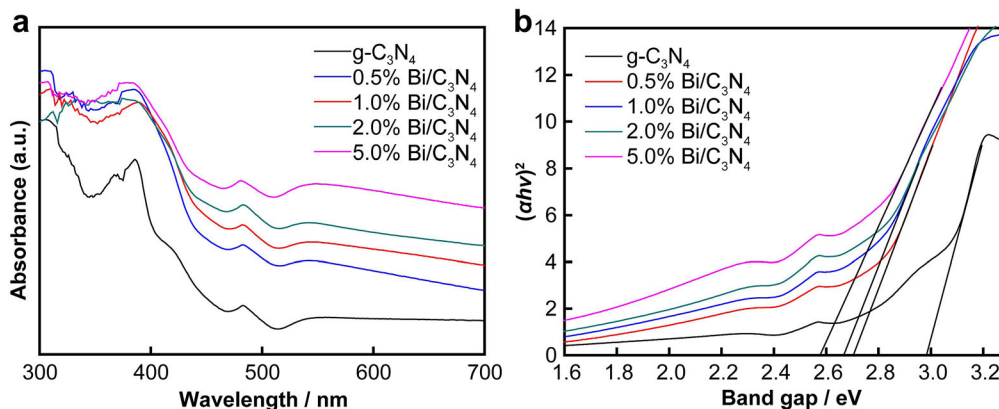

Fig. 3 a UV–Vis diffuse reflectance spectra and b estimated band gap obtained from K-M equation of g-C_3N_4 and x% Bi/C_3N_4
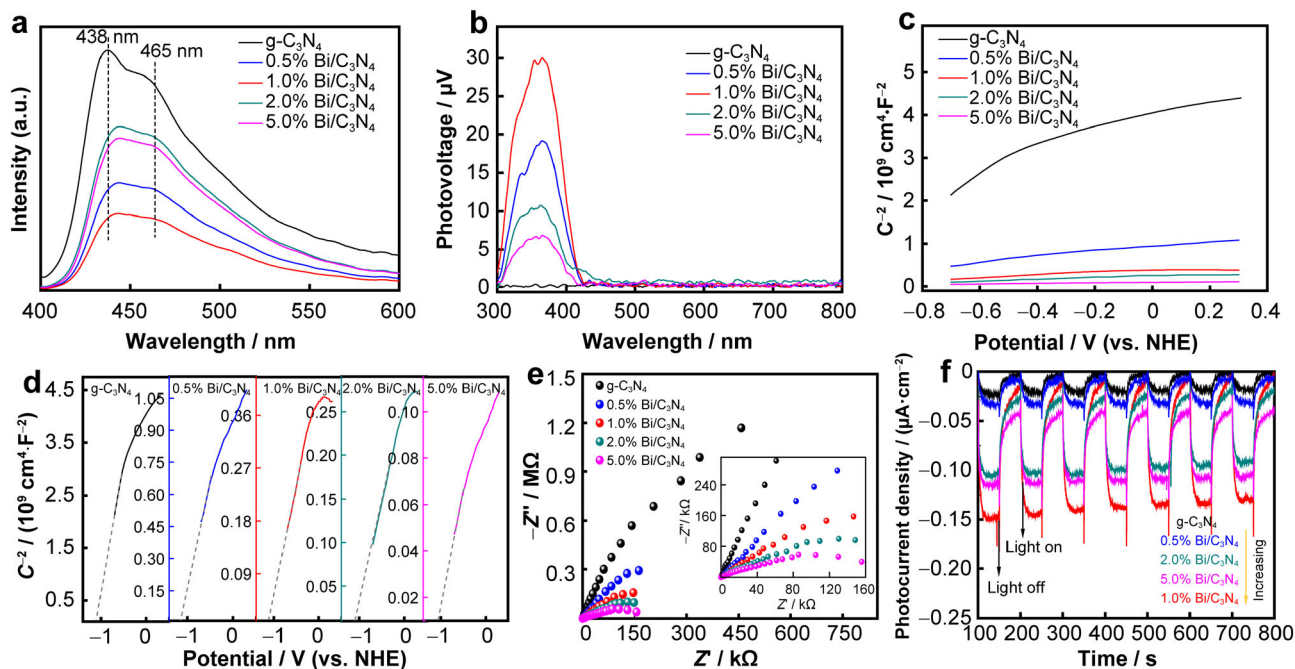
Fig. 4 **a** PL spectra; **b** SPV spectra; **c** Mott–Schottky plots and **d** partial enlargement; **e** electrochemical impedance spectroscopy and **f** photocurrent intensity of g-C_3N_4 and $x\%$ Bi/C_3N_4

To further verify the photogenerated charge migration behavior at the interface between g-C_3N_4 and $x\%$ Bi/C_3N_4, surface photovoltage tests were performed, and the results are displayed in Fig. 4b. In n-type semiconductors, the photogenerated holes generated under illumination move toward the surface under the action of a self-built electric field, thus forming a positive potential difference [41]. After the loading of Bi nanospheres, the positive photovoltage signal of all the samples became stronger, representing a higher charge separation efficiency. This phenomenon confirms the capture effect of the Bi metal on the photogenerated electrons.

By evaluating the photoelectrochemical characteristics, the separation and transfer mechanism of charge carriers at the interface after Bi metal is loaded on the surface of g-C_3N_4 can be better understood. The Mott–Schottky curves of g-C_3N_4 and 1.0% Bi/C_3N_4 are shown in Fig. 4c. The positive slope of the M–S curve reflects the characteristics of the n-type semiconductor. In addition, the carrier concentration of the material can be estimated from the M–S curve that is negatively correlated with the slope [42]. As Bi loading increased, the carrier concentration of the sample gradually increased. This is related to the metallic properties of the loaded Bi nanospheres, which allow more free electrons to participate in the generation of ROS.

The tangent of the curve intersects with the x-axis, and the intersection point can be roughly determined as the flat band potential (E_{fb}) of the material. Based on the test results versus the saturated calomel electrode potential, the E_{fb} value of g-C_3N_4 and 1.0% Bi/C_3N_4 was determined to be -1.13 eV (vs. NHE) according to the empirical formula [43], as shown in Fig. 4d. In n-type semiconductors, E_{fb} is roughly located at the edge of the conduction band [44]; hence, the conduction band potential of g-C_3N_4 and 1.0% Bi/C_3N_4 is ~ -1.13 V (vs. NHE), which is higher than the Fermi level of metallic Bi (-0.17 eV vs. NHE). Therefore, when Bi is in contact with g-C_3N_4, a Schottky barrier is formed at their contact interface [45]. The photogenerated electrons excited under visible-light illumination can quickly be transferred from the conduction band of g-C_3N_4 to the surface of Bi nanospheres, thereby promoting the directional migration of electrons and participating in the formation of ROS on the surface for photocatalytic antibacterial activity.

The effect of the Bi/C_3N_4 composite structure on the charge transfer kinetics at the interface was further analyzed by electrochemical impedance, and the electrochemical impedance spectra of g-C_3N_4 and $x\%$ Bi/C_3N_4 are illustrated in Fig. 4e. The size of the arc radius represents the charge transfer rate on the electrode. The smaller the radius is, the smaller the resistance is, which indicates a higher charge transfer efficiency [46]. The arc radius of $x\%$ Bi/C_3N_4 became smaller than that of g-C_3N_4 with the increase in Bi loading, as shown in Fig. 4e, representing a smaller impedance, which reveals that the Schottky junction formed between Bi and g-C_3N_4 is more conducive to the separation and transfer of charge carriers.

The amperometric I–t method under visible light was used to detect the light response capability and carrier separation efficiency of the samples. Figure 4f shows the transient photocurrent response spectra of g-C$_3$N$_4$ and x% Bi/C$_3$N$_4$ upon exposure to visible light for 50 s under a bias of 0 V (vs. SCE). It can be observed that all Bi-loading samples have a higher photocurrent density than g-C$_3$N$_4$, and 1.0% Bi/C$_3$N$_4$ exhibits the highest photocurrent density, suggesting that Bi nanospheres can capture electrons from g-C$_3$N$_4$ to promote the separation of photogenerated carriers at the interface. The photocurrent density maintained a high degree of stability during multiple cycles of light on and off, signifying that the photogenerated carriers have a stable separation efficiency. It is worth noting that with the increase in Bi loading, the dark current of the samples gradually increased, which is related to the increase in carrier concentration of the materials and the decrease in their impedance [47]. Consequently, loading Bi nanospheres on the surface of g-C$_3$N$_4$ would enhance the separation and transfer efficiency of its charge carriers according to the above electrochemical performance analysis.

3.4 Photocatalytic antibacterial properties

The photocatalytic bactericidal activity of g-C$_3$N$_4$ and 1.0% Bi/C$_3$N$_4$ was evaluated in phosphate buffer solution (PB, 0.1 mol·L^{-1}, pH 7.0) under visible-light irradiation ($\lambda \geq 420$ nm). Diffusion plate experiments intuitively present different antibacterial properties of the two samples against *E. coli*. According to the number of growing colonies, 1.0% Bi/C$_3$N$_4$ exhibited better antibacterial performance than g-C$_3$N$_4$ by inactivating *E. coli* (Fig. 5) after

1-h illumination. As shown in Fig. 6b, c, the photocatalytic activity of 1.0% Bi/C$_3$N$_4$ was approximately nine times higher than that of pristine g-C$_3$N$_4$, achieving a 96.4% sterilization efficiency toward *E. coli* within 60 min, whereas pristine g-C$_3$N$_4$ only achieved 12.3% inactivation. Meanwhile, the bactericidal activity of g-C$_3$N$_4$ and 1.0% Bi/C$_3$N$_4$ was negligible (Fig. 6a) under dark conditions, suggesting that the enhanced photocatalytic bactericidal activity of 1.0% Bi/C$_3$N$_4$ is not related to the toxicity of Bi loading at C$_3$N$_4$. Cytotoxicity was determined by cell live/dead staining assays, and the live/dead staining fluorescence images of osteoblasts cultured on the samples for 1 and 3 days are shown in Fig. 7a. These fluorescence staining results directly confirmed that all the samples could support fibroblast growth without appreciable cytotoxicity. In addition, the MTT assay was performed to evaluate the cytotoxicity of the samples, and the results are shown in Fig. 7b. This assay demonstrated that cells cultured on x% Bi/C$_3$N$_4$ exhibited relatively higher viability than those cultured on g-C$_3$N$_4$ throughout the incubation period, and the results are consistent with staining fluorescence. The bismuth nanospheres improved the proliferation of fibroblast due to the increased surface area of Bi/C$_3$N$_4$ and its non-toxic characteristics.

In the photocatalytic reaction, the electrons and holes generated by light-excited g-C$_3$N$_4$ react with O$_2$ and H$_2$O to form ROS, including superoxide radicals (·O$_2^-$), hydrogen peroxide (H$_2$O$_2$), and hydroxyl radicals (·OH). These reactive oxygen species diffuse into the solution and attack the bacteria surrounding the photocatalyst, causing their inactivation. Among them, 1.0% Bi/C$_3$N$_4$ presented the highest sterilization efficiency against *E. coli* under the same conditions, and on the basis of previous reports, the
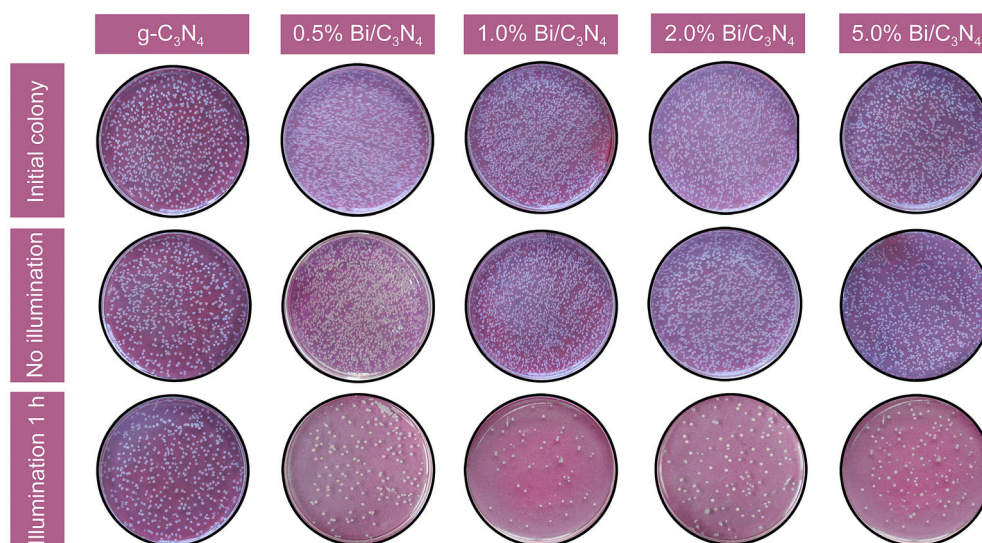

Fig. 5 Antibacterial activity characterization of samples toward *E. coli*: standard colony counting plate results of different samples without and with visible-light illumination
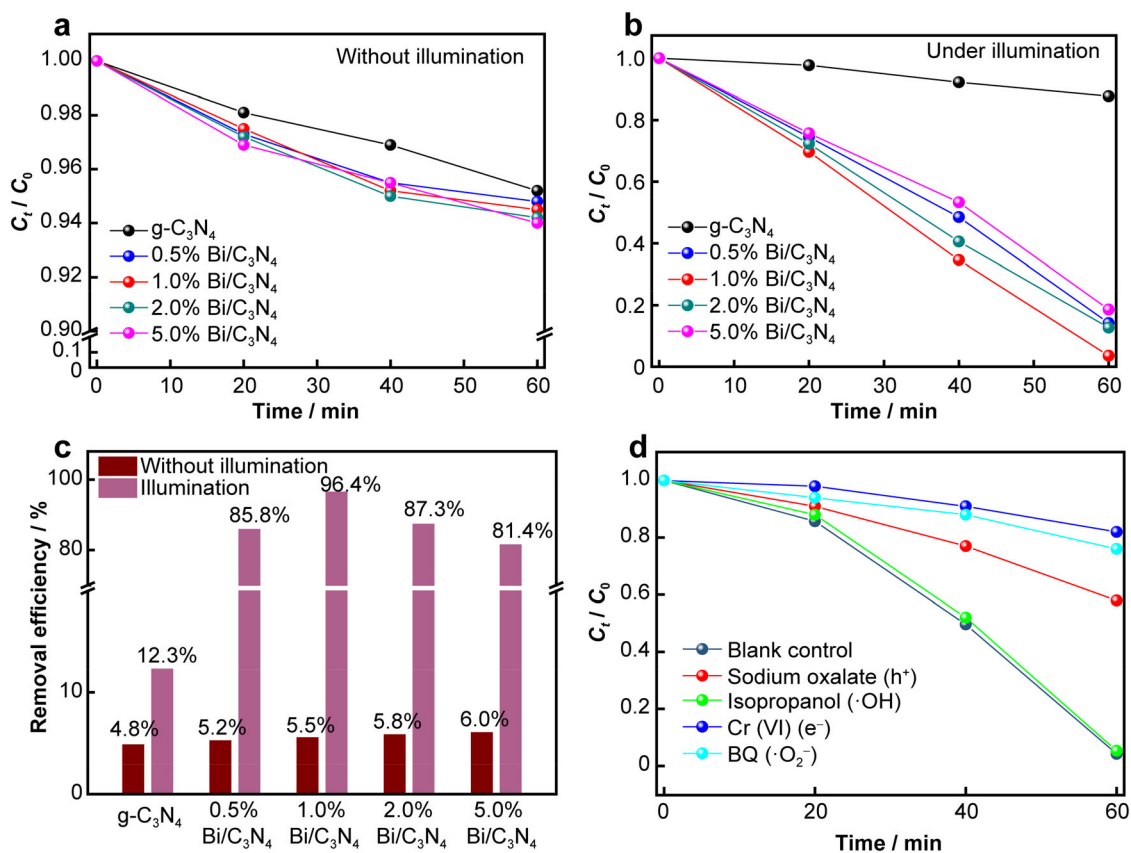
Fig. 6 a Bactericidal activity of g-C$_3$N$_4$ and x% Bi/C$_3$N$_4$ towards *E.coli* without visible-light illumination and **b** under visible-light illumination ($\lambda \geq 420$ nm); **c** bacterial removal efficiency of prepared samples under visible-light illumination; **d** photocatalytic disinfection performance of 1.0% Bi/C$_3$N$_4$ composite towards *E.coli* under visible light illumination for 60 min in presence of different scavengers

photocatalytic antibacterial performance of 1.0% Bi/C$_3$N$_4$ in this study is superior to that of many Ag- or Bi-based photocatalysts, as shown in Table 1 [48–55]. These results strongly indicate that stabilizing Bi nanospheres on the g-C$_3$N$_4$ support and realizing the best synergy between them is crucial for significantly boosting the antibacterial performance. In spite of this, excessive Bi greatly reduced the utilization of visible light by g-C$_3$N$_4$ due to the absorption of most of the incident light, resulting in a decrease in the photocatalytic activity of 2.0% and 5.0% Bi/C$_3$N$_4$.

3.5 Antibacterial mechanism

It is well known that the generation of reactive oxidative species is the main factor responsible for photocatalytic disinfection. Therefore, different scavengers were added to the photocatalytic reaction system to further determine which reactive oxidative species play a pivotal role in Bi/C$_3$N$_4$ photocatalytic disinfection under visible-light illumination. Accordingly, sodium oxalate (2 mmol·L^{-1}), isopropanol (0.5 mmol·L^{-1}), benzoquinone (BQ,

1 mmol·L^{-1}), and Cr (VI) (0.05 mmol·L^{-1}) were used to trap h$^+$, ·OH, ·O$_2^-$, and e$^-$, respectively. All scavengers have been reported to exert no toxicity to *E. coli* at this concentration level [56]. Fig. 6d shows the disinfection performance of samples with different scavengers added after 60-min visible-light illumination. Taking the disinfection process without scavenger as a control, the disinfection effect of isopropanol as the ·OH scavenger was basically unchanged, indicating that ·OH has no effect on the antibacterial activity, which is ascribed to the valence band of g-C$_3$N$_4$ ($\sim$ 1.46 eV) incapable of producing ·OH (E^θ(H$_2$O/·OH) = 2.38 V (vs. NHE)). The photocatalytic disinfection effect changed slightly after adding sodium oxalate, suggesting that the role of h$^+$ in the g-C$_3$N$_4$ valence band is not very important in the photocatalytic process. Significantly, the presence of BQ and Cr(VI) remarkably reduced the antibacterial performance, revealing that ·O$_2^-$ is the key active substance in the photocatalytic disinfection process, and e$^-$ can activate O$_2$ to generate ·O$_2^-$.

A plausible photocatalytic mechanism of Bi/C$_3$N$_4$ with enhanced antibacterial activity is proposed based on the
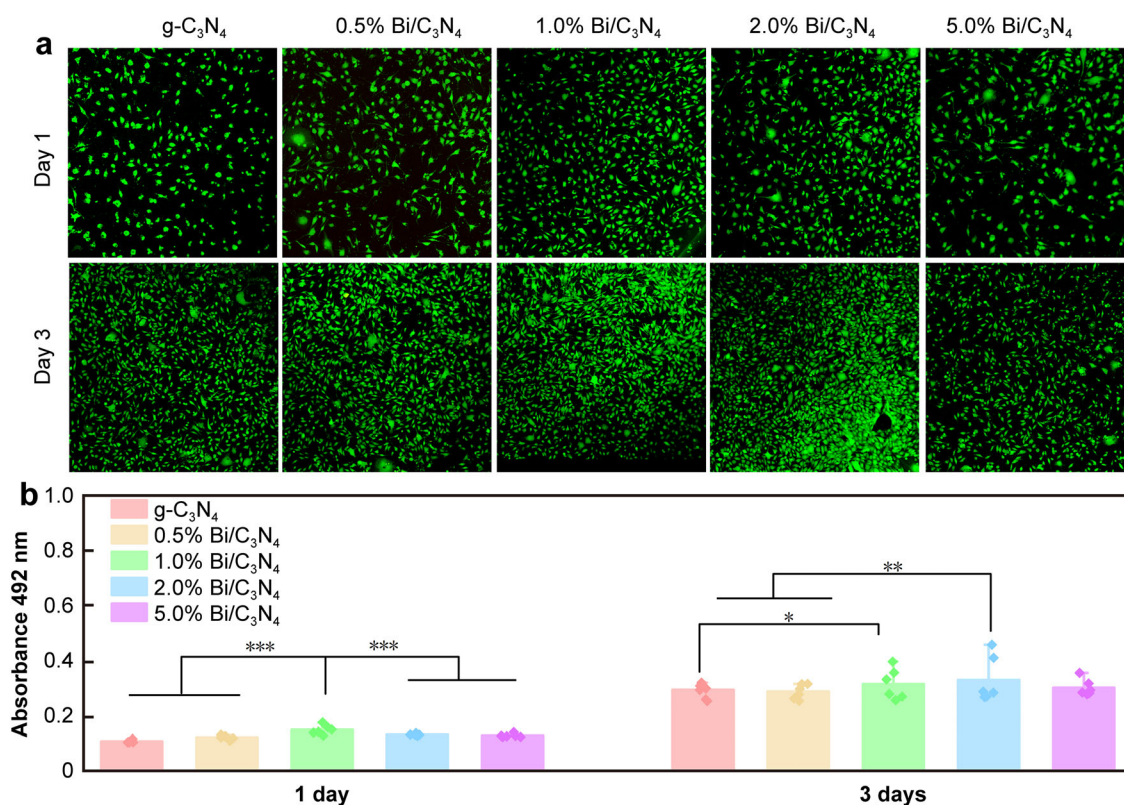
Fig. 7 a Fluorescence images of live/dead staining of fibroblast afterculturing for 1 and 3 days on g-C_3N_4 and x% Bi/C_3N_4; **b** MTT assay of fibroblast seeded on different samples for 1 and3 days (error bars indicatinge means $\pm$ standard deviations: **$P < 0.01$ and *** $P < 0.001$)

Table 1 Comparison of *E. coli* inactivation ability between 1.0% Bi/C_3N_4 and other materials

Catalyst	Reaction conditions	Time	Removal rate/%	Refs.
Ag/g-C_3N_4	300-W xenon lamp ($\lambda > 400$ nm)	2 h	100	[48]
PCNSs	500-W xenon lamp	2 h	96.5	[49]
g-C_3N_4	300-W xenon lamp ($\lambda > 400$ nm)	4 h	100	[50]
g-C_3N_4/TiO_2	300-W Xe lamp ($\lambda > 420$ nm), 30 mW·cm^{-2}	3 h	100	[51]
Bi_2O_3/Bi_2MoO_6	300-W xenon lamp ($\lambda > 420$ nm)	5 h	100	[52]
AgI/$BiVO_4$	A 300-W Xe lamp ($\lambda > 420$ nm)	50 min	100	[53]
P/Ag/Ag_2O/Ag_3PO_4/TiO_2	LED lamps (750 W·m^{-2})	40 min	100	[54]
AgFeNTFS	Visible-light irradiation	2 h	100	[55]
1.0% Bi/C_3N_4	300-W xenon lamp ($\lambda > 420$ nm)	1 h	96.4	This work

above experimental results. Bi was loaded onto the g-C_3N_4 sheets to form an interface g-C_3N_4. The Bi nanospheres on the g-C_3N_4 sheets take effect in two ways. Under visible-light irradiation, the photogenerated electrons transition to the conduction band, and the photogenerated holes remain in the valence band. Because g-C_3N_4 contacts Bi to form a Schottky junction, the electrons on the CB of g-C_3N_4 tend to be transferred to Bi to balance the Fermi level between

g-C_3N_4 and Bi, so that the electron energy on the surface of g-C_3N_4 is higher than that inside the semiconductor. The Schottky barrier formed at the interface between g-C_3N_4 and Bi improves the separation efficiency of the photo-generated electrons and holes, enhancing the photocatalytic performance of g-C_3N_4. Moreover, the SPR effect of Bi nanospheres under visible-light illumination drives the visible-light absorption range to ~ 500 nm, which notably
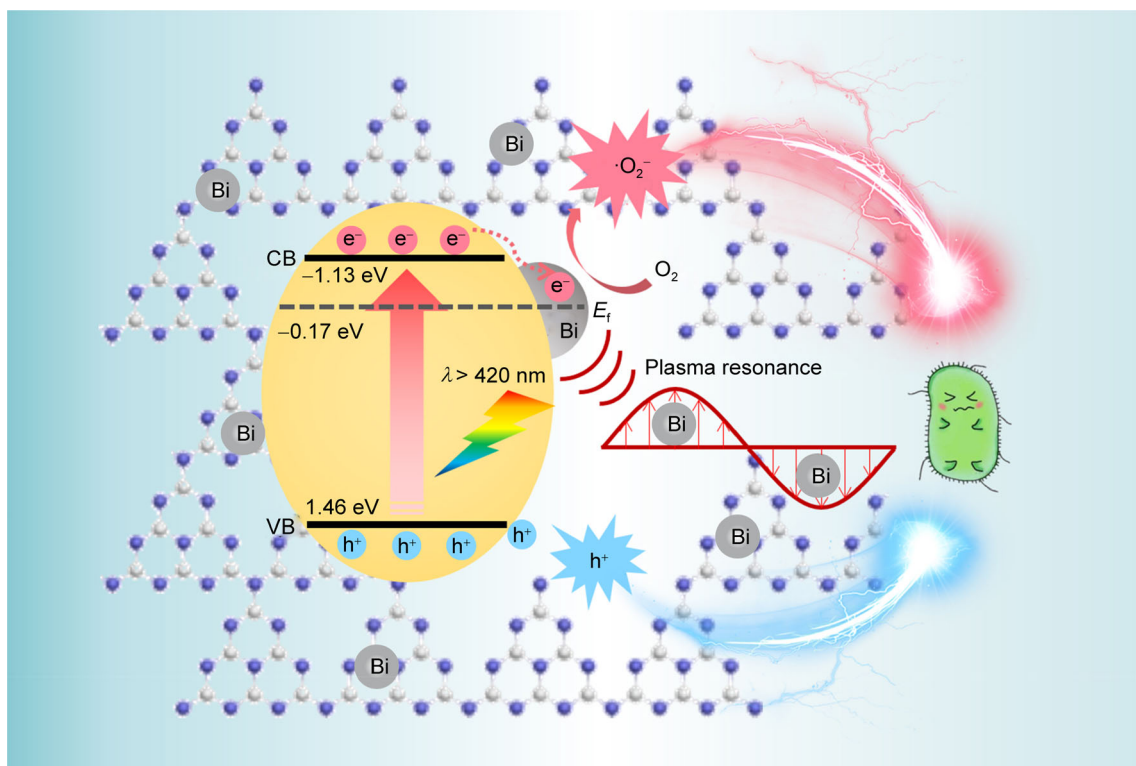
Fig. 8 Plausible mechanism of enhanced antibacterial photocatalytic performance Bi-loaded g-C$_3$N$_4$

promotes the light utilization efficiency of the composite material. As shown in Fig. 8, the Fermi level of Bi is $\sim$ -0.17 eV. The conduction band of g-C$_3$N$_4$ is more negative than that of Bi. Thermodynamically, the photoexcited electrons generated in the conduction band of g-C$_3$N$_4$ are transferred to the Bi nanospheres, while promoting the more effective transfer of h$^+$ excited by the light of g-C$_3$N$_4$ itself simultaneously, which can be used as ROS to inactivate bacteria to a certain extent. According to the trapping experiment, as the main active species in the photocatalytic disinfection process, $\cdot$O$_2{}^-$ is mainly produced by the activation of O$_2$ by e$^-$ on CB. The higher levels of $\cdot$O$_2{}^-$ indicate the facilitation of electron separation and transfer by Bio. The strong oxidation activity of $\cdot$O$_2{}^-$ produced in large quantities attacks the cell membrane, causing the leakage of cytosol and finally kills the bacteria.

4 Conclusion

A novel Bi/C$_3$N$_4$ nanocomposite was prepared by loading elemental Bi nanospheres onto the surface of g-C$_3$N$_4$. The composite material exhibited more efficient photogenerated charge separation and transfer efficiency than pristine g-C$_3$N$_4$, thereby contributing to the generation of ROS. The SPR effect of metallic Bi also led to enhanced light absorption in the visible-light region. The synergy of multiple advantages resulted in the enhanced photocatalytic antibacterial activity of Bi/C$_3$N$_4$. Among them, 1.0% Bi/C$_3$N$_4$ exhibited the best removal efficiency of 96.4% for *E. coli* under 1-h visible-light irradiation. This work provides a new type of photocatalyst with great application potential for photocatalytic antibacterial applications.

Declarations

Conflict of interests The authors declare that they have no conflict of interest.

References

[1] Dhand C, Venkatesh M, Barathi VA, Harini S, Bairagi S, Leng EGT, Muruganandham N, Low KZW, Fazil MHUT, Loh XJ, Srinvasan DK, Liu SP, Beuerman RW, Verma NK, Ramakrishna S, Lakshminarayanan R. Bio-inspired crosslinking and matrix-drug interactions for advanced wound dressings with long-term antimicrobial activity. Biomaterials. 2017;138:153.

[2] Macvane SH. Antimicrobial resistance in the intensive care unit: a focus on gramnegative bacterial infections. J Intensive Care Med. 2017;32(1):25.

[3] Mao C, Xiang Y, Liu X, Cui Z, Yang X, Li Z, Zhu S, Zheng Y, Yeung KWK, Wu S. Repeatable photodynamic therapy with triggered signaling pathways of fibroblast cell proliferation and differentiation to promote bacteria-accompanied wound healing. ACS Nano. 2018;12(2):1747.

[4] Yu X, Wang S, Zhang X, Qi A, Qiao X, Liu Z, Wu M, Li L, Wang ZL. Heterostructured nanorod array with piezophototronic and plasmonic effect for photodynamic bacteria killing and wound healing. Nano Energy. 2018;46:29.

[5] Liu WY, Zuo RT, Zhu TL, Zhu M, Zhao SC, Zhu YF. Forsterite-hydroxyapatite composite scaffolds with photothermal antibacterial activity for bone repair. J Adv Ceram. 2021;10(5):1095.

[6] He W, Kim HK, Wamer WG, Melka D, Callahan JH, Yin JJ. Photogenerated charge carriers and reactive oxygen species in ZnO/Au hybrid nanostructures with enhanced photocatalytic and antibacterial activity. J Am Chem Soc. 2013;136(2):750.

[7] Tabunag JS, Guo YJ, Yu HZ. Interactions between hemin-binding DNA aptamers and hemin-graphene nanosheets: reduced affinity but unperturbed catalytic activity. J Anal Test. 2019;3:107.

[8] Ding HY, Han DL, Han YJ, Liang YQ, Liu XM, Li ZY, Zhu SL, Wu SL. Visible light responsive CuS/protonated g-C_3N_4 heterostructure for rapid sterilization. J Hazard Mater. 2020;393:122423.

[9] Zhao XH, Li BX, Wei C, Wang XB, Zhou JG, Lou XD. Flower-like Ag/ZnO synthesized by one pot hydrothermal method at low temperature with enhanced sunlight photocatalytic performance. Chin J Rare Metals. 2019;43(6):621.

[10] Tian L, Li J, Liang F, Wang J, Wang JK, Li SS, Zhang HJ, Zhang S. Molten salt synthesis of tetragonal carbon nitride hollow tubes and their application for removal of pollutants from wastewater. Appl Catal B Environ. 2018;225:307.

[11] Jing L, Zhu R, Phillips DL, Yu JC. Effective prevention of charge trapping in graphitic carbon nitride with nanosized red phosphorus modification for superior photo (electro) catalysis. Adv Funct Mater. 2017;27(46):1703484.

[12] Wu BB, Li Y, Su K, Tan L, Xiang YM, Xiang YM, Liu XM, Cui ZD, Yang XJ, Liang YQ, Li ZY, Zhu SL, Wu KWK, Wu SL. The enhanced photocatalytic properties of MnO_2/g-C_3N_4 heterostructure for rapid sterilization under visible light. J Hazard Mater. 2019;377:227.

[13] Yuan D, Huang LY, Li YP, Wang H, Xu XQ, Wang CB, Yang L. A novel AgI/BiOI/pg-C_3N_4 composite with enhanced photocatalytic activity for removing methylene orange, tetracycline and *E. Coli*. Dyes Pigm. 2020;177:108253.

[14] Liu WW, Pan J, Peng RF. Shape-dependent hydrogen generation performance of PtPd bimetallic co-catalyst coupled with C_3N_4 photocatalyst. Rare Met. 2021;40(12):3554.

[15] Huang S, Ouyang T, Zheng BF, Dan M, Liu ZQ. Enhanced photoelectrocatalytic activities for CH_3OH-to-HCHO conversion on Fe_2O_3/MoO_3: Fe-O-Mo covalency dominates the intrinsic activity. Angew Chem Int Ed. 2021;60(17):9546.

[16] He Y, Yan C, Chen XZ, Wang Z, Ouyang T, Guo ML, Liu ZQ. Construction of core-shell heterojunction regulating α-Fe_2O_3 layer on CeO_2 nanotube arrays enables highly efficient Z-scheme photoelectrocatalysis. Appl Catal B Environ. 2020;276:119138.

[17] Wei RB, Huang ZL, Gu GH, Wang Z, Zeng LX, Chen YB, Liu ZQ. Dual-cocatalysts decorated rimous CdS spheres advancing highly-efficient visible-light photocatalytic hydrogen production. Appl Catal B Environ. 2018;231:101.

[18] Huang S, Zheng BF, Tang ZY, Mai XQ, Ouyang T, Liu ZQ. CH_3OH selective oxidation to HCHO on Z-scheme Fe_2O_3/g-C_3N_4 hybrid: the rate-determining step of C-H bond scission. Chem Eng J. 2021;422:130086.

[19] Zheng NC, Ouyang T, Chen YB, Wang Z, Chen DY, Liu ZQ. Ultrathin CdS shell-sensitized hollow S-doped CeO_2 spheres for efficient visible-light photocatalysis. Catal Sci Technol. 2019;9(6):1357.

[20] Shen QQ, Xue JB, Li Y, Gao GX, Li Q, Liu XG, Jia HS, Xu BS, Wu YC, Dillon SJ. Construction of CdSe polymorphic junctions with coherent interface for enhanced photoelectrocatalytic hydrogen generation. Appl Catal B Environ. 2021;282:119552.

[21] Yang YX, Guo YN, Liu FY, Yuan X, Guo YH, Zhang SQ, Guo W, Huo MX. Preparation and enhanced visible-light photocatalytic activity of silver deposited graphitic carbon nitride plasmonic photocatalyst. Appl Catal B Environ. 2013;142:828.

[22] Walmsley JD, Hill JW, Saha P, Hill CM. Probing electrocatalytic CO_2 reduction at individual Cu nanostructures via optically targeted electrochemical cell microscopy. J Anal Test. 2019;3:140.

[23] Marschall R. Semiconductor composites: strategies for enhancing charge carrier separation to improve photocatalytic activity. Adv Funct Mater. 2014;24(17):2421.

[24] Liu CC, Wang L, Xu H, Wang S, Gao SM, Ji XC, Xu Q, Lan W. "One pot" green synthesis and the antibacterial activity of g-C_3N_4/Ag nanocomposites. Mater Lett. 2016;164:567.

[25] Gil-Allué C, Tlili A, Schirmer K, Gessner MO, Behra R. Long-term exposure to silver nanoparticles affects periphyton community structure and function. Environ Sci Nano. 2018;5(6):1397.

[26] Dong F, Xiong T, Sun YJ, Zhao ZW, Zhou Y, Feng X, Wu ZB. A semimetal bismuth element as a direct plasmonic photocatalyst. Chem Commun. 2014;50(72):10386.

[27] Pathak A, Blair VL, Ferrero RL, Mehring M, Andrews PC. Bismuth(III) benzohydroxamates: powerful anti-bacterial activity against Helicobacter pylori and hydrolysis to a unique Bi_{34} oxido-cluster $[Bi_{34}O_{22}(BHA)_{22}(H\text{-}BHA)_{14}(DMSO)_6]$. Chem Commun. 2014;50(96):15232.

[28] Qin F, Li GF, Xiao H, Lu Z, Sun HZ, Chen R. Large-scale synthesis of bismuth hollow nanospheres for highly efficient Cr(VI) removal. Dalton Trans. 2012;41(37):11263.

[29] Wang XC, Maeda K, Thomas A, Takanabe K, Xin G, Carlsson JM, Domen K, Antonietti M. A metal-free polymeric photocatalyst for hydrogen production from water under visible light. Nat Mater. 2009;8(1):76.

[30] Xiao J, Yang WY, Li Q. Bi quantum dots on rutile TiO_2 as hole trapping centers for efficient photocatalytic bromate reduction under visible light illumination. Appl Catal B Environ. 2017;218:111.

[31] Swy ER, Schwartz-Duval AS, Shuboni DD, Latourette MT, Mallet CL, Parys M, Cormode DP, Shapiro EM. Dual-modality, fluorescent, plga encapsulated bismuth nanoparticles for molecular and cellular fluorescence imaging and computed tomography. Nanoscale. 2014;6(21):13104.

[32] Vinu A. Two-dimensional hexagonally-ordered mesoporous carbon nitrides with tunable pore diameter, surface area and nitrogen content. Adv Funct Mater. 2008;18(5):816.

[33] Zhang JS, Zhang MW, Zhang GG, Wang WC. Synthesis of carbon nitride semiconductors in sulfur flux for water photoredox catalysis. ACS Catal. 2012;2(6):940.

[34] Wang JJ, Ren YM, Chen MH, Cao GX, Chen ZJ, Wang P. Bismuth hollow nanospheres for efficient electrosynthesis of ammonia under ambient conditions. J Alloy Compd. 2020;830:154668.

[35] Bai XJ, Zong RL, Li CX, Liu D, Liu YF, Zhu YF. Enhancement of visible photocatalytic activity via Ag@C_3N_4 core-shell plasmonic composite. Appl Catal B Environ. 2014;147:82.

[36] Yang W, Zhang L, Xie J, Zhang X, Liu Q, Yao T, Wei S, Zhang Q, Xie Y. Enhanced photoexcited carrier separation in

oxygen-doped ZnIn$_2$S$_4$ nanosheets for hydrogen evolution. Angew Chem Int Ed. 2016;55(23):6716.

[37] Xue JB, Ma T, Shen QQ, Guan RF, Jia HS, Liu XG, Xu BS. A novel synthesis method for Ag/g-C$_3$N$_4$ nanocomposite and mechanism of enhanced visible-light photocatalytic activity. J Mater Sci Mater El. 2019;30(16):15636.

[38] Jiang GM, Li XW, Lan MN, Shen T, Lv XS, Dong F, Zhang S. Monodisperse bismuth nanoparticles decorated graphitic carbon nitride: enhanced visible-light-response photocatalytic NO removal and reaction pathway. Appl Catal B Environ. 2017;205:532.

[39] Guo LT, Cai YY, Ge JM, Zhang YN, Gong LH, Li XH, Wang KX, Ren QZ, Su J, Chen JS. Multifunctional Au/Co@CN nanocatalyst for highly efficient hydrolysis of ammonia borane. ACS Catal. 2015;5(1):388.

[40] Dong F, Zhao Z, Sun Y, Zhang YX, Yan S, Wu ZB. An advanced semimetal-organic Bi spheres-g-C$_3$N$_4$ nanohybrid with SPR-enhanced visible-light photocatalytic performance for NO purification. Environ Sci Technol. 2015;49(20):12432.

[41] Xie TF, Wang DJ, Zhu LJ, Wang C. Application of surface photovoltage technique to the determination of conduction types of azo pigment films. J Phys Chem B. 2000;104(34):8177.

[42] Zhang WJ, Shen QQ, Xue JB, Li Q, Liu XG, Jia HS. Preparation and photoelectrochemical water oxidation property of hematite nanobelts containing highly ordered oxygen vacancies. J Inorg Mater. 2021. https://doi.org/10.15541/jim20210175.

[43] Gao JQ, Xue JB, Jia SF, Shen QQ, Zhang XC, Jia HS, Liu XG, Li Q, Wu YC. Self-doping surface oxygen vacancy-induced lattice strains for enhancing visible light-driven photocatalytic H$_2$ evolution over black TiO$_2$. ACS Appl Mater Inter. 2021; 13(16):18758.

[44] Ong WJ, Putri LK, Tan YC, Tan LL, Li N, Ng YH, Wen XM, Chai SP. Unravelling charge carrier dynamics in protonated g-C$_3$N$_4$ interfaced with carbon nanodots as co-catalysts toward enhanced photocatalytic CO$_2$ reduction: a combined experimental and first-principles DFT study. Nano Res. 2017;10(5):1673.

[45] Zhang XM, Chen YL, Liu RS, Tsai DP. Plasmonic photocatalysis Rep Prog Phys. 2013;76(4):46401.

[46] Gao JQ, Xue JB, Shen QQ, Liu TW, Zhang XC, Liu XG, Jia HS, Li Q, Wu YC. A promoted photocatalysis system trade-off between thermodynamic and kinetic via hierarchical distribution dual-defects for efficient H$_2$ evolution. Chem Eng J. 2020. https://doi.org/10.1016/j.cej.2021.133281.

[47] Gao JQ, Shen QQ, Guan RF, Xue JB, Liu XG, Jia HS, Li Q, Wu YC. Oxygen vacancy self-doped black TiO$_2$ nanotube arrays by aluminothermic reduction for photocatalytic CO$_2$ reduction under visible light illumination. J CO$_2$ Util. 2020;35:205.

[48] Wei F, Li JD, Dong CC, Bi YJ, Han XJ. Plasmonic Ag decorated graphitic carbon nitride sheets with enhanced visible-light response for photocatalytic water disinfection and organic pollutant removal. Chemosphere. 2020;242:125201.

[49] He NN, Cao SH, Zhang LH, Tian ZD, Chen H, Jiang F. Enhanced photocatalytic disinfection of *Escherichia coli* K-12 by porous g-C$_3$N$_4$ nanosheets: combined effect of photo-generated and intracellular ROSs. Chemosphere. 2019;235:1116.

[50] Huang JH, Ho W, Wang XC. Metal-free disinfection effects induced by graphitic carbon nitride polymers under visible light illumination. Chem Commun. 2014;50(33):4338.

[51] Li GY, Nie X, Chen JY, Jiang Q, An TC, Wong PK, Zhang HM, Zhao HJ, Yamashita H. Enhanced visible-light-driven photocatalytic inactivation of Escherichia coli using g-C$_3$N$_4$/TiO$_2$ hybrid photocatalyst synthesized using a hydrothermal-calcination approach. Water Res. 2015;86:17.

[52] Shi HX, Wang CJ, Wang W, Hu XY, Fan J, Tang ZS. The enhanced visible light driven photocatalytic inactivation of Escherichia coli with Z-Scheme Bi$_2$O$_3$/Bi$_2$MoO$_6$ heterojunction and mechanism insight. Ceram Int. 2021;47(6):7974.

[53] Guan DL, Niu CG, Wen XJ, Guo H, Deng CH, Zeng GM. Enhanced Escherichia coli inactivation and oxytetracycline hydrochloride degradation by a Z-scheme silver iodide decorated bismuth vanadate nanocomposite under visible light irradiation. J Colloid Interf Sci. 2018;512:272.

[54] Liu N, Zhu Q, Zhang N, Zhang C, Kawazoe N, Chen GP, Negishi N, Yang YN. Superior disinfection effect of *Escherichia coli* by hydrothermal synthesized TiO$_2$-based composite photocatalyst under LED irradiation: influence of environmental factors and disinfection mechanism. Environ Pollut. 2019;247:847.

[55] He JH, Zeng XK, Lan SY, Lo IMC. Reusable magnetic Ag/Fe, N-TiO$_2$/Fe$_3$O$_4$@SiO$_2$ composite for simultaneous photocatalytic disinfection of *E. coli* and degradation of bisphenol A in sewage under visible light. Chemosphere. 2019;217:869.

[56] Wang W, Yu Y, An T, Li G, Yip HY, Yu JC, Wong PK. Visible-light-driven photocatalytic inactivation of *E. coli* K-12 by bismuth vanadate nanotubes: bactericidal performance and mechanism. Environ Sci Technol. 2012;46(8):4599.